Size-dependent lattice dynamics of barium titanate nanoparticles

2007 J. Phys.: Condens. Matter 19 476212

(http://iopscience.iop.org/0953-8984/19/47/476212)

IOP PUBLISHING JOURNAL OF PHYSICS: CONDENSED MATTER

J. Phys.: Condens. Matter **19** (2007) 476212 (12pp) doi:10.1088/0953-8984/19/47/476212

Size-dependent lattice dynamics of barium titanate nanoparticles

Tung-Ching Huang[1], **Mei-Tan Wang**[1], **Hwo-Shuenn Sheu**[2] **and Wen-Feng Hsieh**[1,3]

[1] Department of Photonics and Institute of Electro-Optical Engineering, National Chiao Tung University, 1001 Tahsueh Road, Hsinchu 30050, Taiwan
[2] National Synchrotron Radiation Research Center, Hsinchu 30076, Taiwan

E-mail: wfhsieh@mail.nctu.edu.tw

Received 10 August 2007, in final form 5 October 2007
Published 1 November 2007
Online at stacks.iop.org/JPhysCM/19/476212

Abstract

By applying a single-tetragonal-phase model to refine the crystal structure and the coupled-phonon model to analyze transverse optical (TO) modes of $BaTiO_3$ nanocrystals, we found, upon decreasing the particle size from 140 to 30 nm, that the tetragonality of $BaTiO_3$ nanocrystallites is reduced accompanied by expanding unit-cell volume, which is the dominant mechanism for reducing giant LO–TO splitting in the $BaTiO_3$ system. The weakening coupling of two low-frequency modes among three A_1 (TO) phonons leads to changing the lowest one from a spectral dip to a peak, whereas the increasing coupling strength between two high-frequency modes repels them farther so that there is less reduction in spectral separation.

1. Introduction

Complex oxide perovskites possessing the ferroelectric property have versatile applications, for example, ceramic capacitors in bulk forms and in the forms of thin films for ferroelectric random access memory, infrared pyroelectric sensors, transistors, microwave electronics, electro-optic modulators, etc. Owning to its excellent ferroelectric properties, barium titanate ($BaTiO_3$) is one of the most generally investigated ferroelectric materials among the complex oxide perovskites [1]. Furthermore, in the continuous advance in miniaturization of ferroelectric devices, $BaTiO_3$ fine particles as a ferroelectric material have been applied in advanced electric devices [2] such as multilayer ceramic capacitors. Their physical properties have been dramatically influenced by various effects, such as temperature [3–5], pressure [4, 6], substitution [7], and size [8–12]. Among them, due to the close relationship between ferroelectric properties and crystal structure, the size dependence of structure is presently the major research topic.

[3] Author to whom any correspondence should be addressed.

By using the Rietveld refinement analysis of x-ray diffraction (XRD) data, the crystal structure with decreasing grain size becomes progressively less tetragonal (c/a becomes close to 1, where c and a are the lattice constants along z and x axes, respectively) at room temperature (RT) and thus shows gradually reducing transition temperature from the tetragonal (ferroelectric) phase to the cubic (paraelectric) phase [8–12]. These phenomena have been numerically investigated assuming that the spurious lattice expansion in perovskite nanocrystals is caused by the surface relaxation [13]. By comparing the observed peak positions and full widths at half maxima (FWHM) of XRD patterns with those of the calculated ones on a cubic lattice containing surface relaxation, Ishikawa *et al* [13] found that the maximum relaxation on the surface of $PbTiO_3$ is about 0.035 and 0.015 nm for $BaTiO_3$.

Because the ferroelectric properties are closely related to the lattice dynamics, Raman spectroscopy provides a valuable technique for this research. By analyzing Raman spectra for $BaTiO_3$ ultrafine particles with grain size < 0.1 μm, Frey *et al* [8] suggested that a locally orthorhombic structure preceded the globally tetragonal form with grain growth. Studies by Yashima *et al* [12] indicated $BaTiO_3$ particles with a size of 40 nm consist of both tetragonal and hexagonal phases. Without considering the mode coupling of transverse optical (TO) phonons, they also suggested the size-induced phase transition occurs between 40 and 30 nm due to increase of the damping factors of phonon modes [11]. However, the ferroelectric transition occurs as a result of a balance between the long-range Coulomb interaction and the short-range force [14]. Coulomb interaction can cause ferroelectric instability due to details of domain structure and defect and boundary conditions [15]. For example, the destructively anharmonic coupling among three TO phonons causes low-frequency Raman spectral dips in both $PbTiO_3$ and $BaTiO_3$ crystals. The anharmonic coupling effect can be distinguished into three individual TO modes [16, 17]. Although there have been a number of Raman studies on the grain size effect [8, 11, 12, 18], it is still not elucidated that a spectral peak rather than a destructive interference dip at 180 cm^{-1} for the A_1 (TO_1) phonon mode was observed with decreasing particle size.

Another direct effect of Coulomb interaction is the splitting of A_1 longitudinal optical (LO) and TO phonons. Via Coulomb interaction, the A_1 (TO_1) mode will couple most strongly with the A_1 (LO_3) mode, that have the same form of atomic displacements in a unit cell of ABO_3 structure. Anomalously large dynamical effective charges give rise to very strong mixing of the mode eigenvectors on going from the TO to the LO case, resulting in a 'giant LO–TO splitting' in the sense that the soft TO mode is most closely related to the hardest LO modes [15]. The calculation of the Born dynamical effective charges, which reflect the local dipole moments developed as atoms are moved, has been performed in ABO_3 cubic perovskite compounds by Zhong *et al* [15]. In the previous study of the $Ba_xSr_{1-x}TiO_3$ (BST) system [7], we elucidated that the repulsion of giant LO–TO splitting with increasing 'Sr' substitution, which causes crystal structure to change from tetragonal phase toward cubic phase, is due to a decrease in the dimensions of the unit cell. In this paper we report, in contrast to that in the BST system, the attractive LO–TO splitting behavior, and depict the low-frequency TO spectral peak along with change of the tetragonal phase toward the cubic one for reducing the diameter of the $BaTiO_3$ nanocrystals from 140 to 30 nm.

2. Experimental details

2.1. Synthesis of $BaTiO_3$ nanoparticles

The glycothermal treatment method [19] was adopted to synthesize $BaTiO_3$ nanocrystals. Barium hydroxide octahydrate ($Ba(OH)_2{\cdot}8H_2O$) was used as the source of Ba and titanium

tetrachloride ($TiCl_4$) was used as the source of Ti. Modification of titanium tetrachloride was achieved by adding deionized (DI) water to prepare transparent aqueous 0.1 M $TiOCl_2$ solution. Amorphous titanium hydrous gel was prepared by adding 30 ml NH_4OH (24%) dropwise into 160 ml 0.1 M $TiOCl_2$ solution at 60 °C for 2 h with stirring. The gel was separated and washed with DI water by three cycles of centrifugation for 4 min at 4000 rpm in a centrifuge. Excess water was decanted after final washing and the wet precursor was redispersed in a mixture of water and 1,4-butanediol. $Ba(OH)_2{\cdot}8H_2O$ was then added into a mixture of water and 1,4-butanediol (1,4-butanediol/deionized water: $B/W = 1$, Ba:Ti molar ratio $= 1$). The total volume of the solvent was 200 ml. The resultant suspension was placed in a 250 ml flask equipped with a stirred head heated to the desired temperature at a rate of 3 °C min^{-1}. To acquire $BaTiO_3$ particles with various grain sizes, reactions were carried out at the desired temperature from 100 to 220 °C for 12 h; the larger sizes of particles require a higher reaction temperature. After glycothermal treatment, the flask was cooled to RT. The powder was then washed with acetic acid solution to remove the residual $BaCO_3$ and the unreacted Ba ions in solution. The removal of residual $BaCO_3$ is crucial because its Raman spectra appear in the range of <200 cm^{-1} [20]. After washing, the recovered powder was dried at 60 °C on a hot plate for 48 h.

2.2. Characterization

The XRD data of the prepared $BaTiO_3$ nanoparticles were collected on the imaging plate with transmission geometry using high intensity synchrotron radiation with wavelength of 0.563 57 Å at beam line BL01C synchrotron radiation facility, NSRRC, in Taiwan. A single-tetragonal-phase ($P4mm$) model was applied to refine the crystal structure with the XRD data by using the Rietveld analysis computer program GSAS (General Structure Analysis System) provided by the National Institute of Standards and Technology (NIST). The morphology of the synthesized particles was observed using field-emission scanning electron microscopy (FESEM, JEOL 6500). The unpolarized Raman spectra were collected by a Spex 1877C triple spectrograph equipped with a liquid-nitrogen-cooled charge-coupled device at 140 K under the excitation of an Ar^+ laser at 488 nm wavelength.

3. Results and discussion

3.1. Microstructure

$BaTiO_3$ nanoparticles shown in the FESEM micrographs of figure 1 have low aggregation and narrow size distribution with mean diameters of about 140, 60, and 30 nm, respectively. To analyze the crystal symmetry of $BaTiO_3$ nanoparticles, high-resolution diffraction patterns of various sizes of $BaTiO_3$ nanoparticles were taken by using high-energy synchrotron radiation x-rays and refined by using the GSAS program; however, to retrench the layout of a printed page, here we just show the refinement result of $BaTiO_3$ with a particle size of 60 nm in figure 2. The XRD profiles around 32.5° in 2θ-scan for all sizes of $BaTiO_3$ particles indicate splitting of (004) and (400) peaks, thus a single-tetragonal-phase ($P4mm$) model was applied to refine the crystal structure with the XRD data. As shown in figure 2, the calculated profiles agree well with the observed ones. The refined structure parameters with very small deviations and reliability (R_{wp}) factors for various sizes of nanoparticles are listed in table 1 and the results are plotted in figure 3. This reveals that the single-tetragonal-phase model is suitable for particle size smaller than 100 nm and even gets better fitting with lower R_{wp} on decreasing particle size. It is consistent with the results of Yoon *et al* [21] that a single tetragonal phase was used for

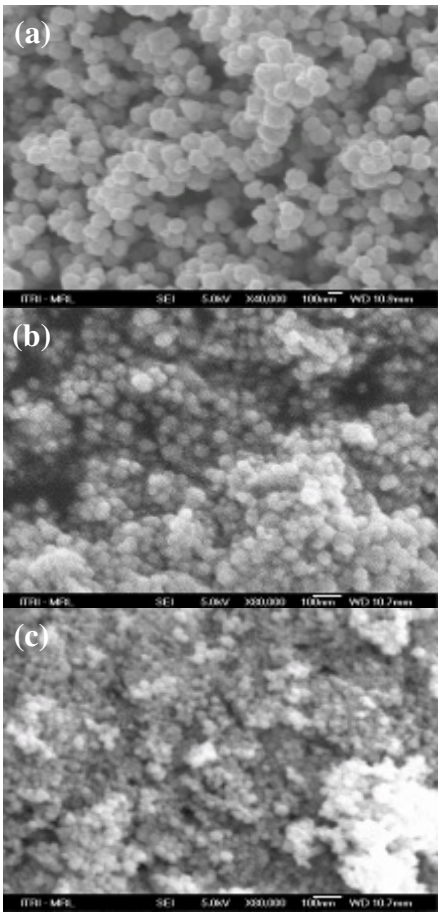

Figure 1. Microstructure (FESEM) of $BaTiO_3$ nanoparticles with average grain size of 140 ± 8 nm (a), 60 ± 6 nm (b) and 30 ± 5 nm (c). The scale bar is 100 nm.

7.5 nm, although Yashima *et al* [12] reported that particles with a size of 40 nm were identified to be a mixture of tetragonal and hexagonal phases. Besides, the ratio c/a is 1.0008 ± 0.0003, which is still greater than 1, reveals that the 30 nm particle is still tetragonal; we will show later that the results of the Raman spectra provide auxiliary evidence that the phonon modes specific to the tetragonal phase of $BaTiO_3$ as described in [23] still appear. We also fitted a cubic model to the XRD pattern of the 30 nm particles. The resultant lattice constant is 4.0341 ± 0.0001 nm and the reliability (R_{wp}) factor is 7.1%, which is acceptable but worse than the 2.78% that fits with the tetragonal model. Furthermore, the larger R-value for the larger particles may result from the fact that preferred orientation may exist in the larger particles, that we did not consider in the refinement.

The lattice constants a and c, shown in figure 3(a), simultaneously relax on decreasing the particle size from 140 to 30 nm. The results also show, consistent with the assumption proposed by Ishikawa *et al* [13], that the tetragonality (c/a) declines from 1.0026 to 1.0008 with expanding unit-cell volume in figure 3(b) as the particle size decreases. The observation is also consistent with the results presented in figure 1 of [11], that c reduces from micrometer size to sub-micrometer size then increases on further decreasing its size, whereas a expands

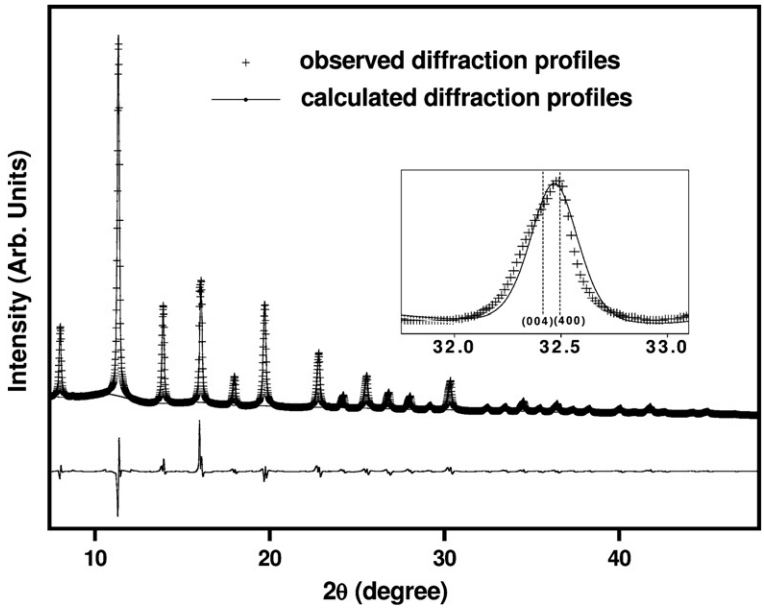

Figure 2. Rietveld pattern of $BaTiO_3$ nanoparticles with average grain size of 60 nm. Observed (cross symbols) and calculated (solid curve) x-ray intensity profiles and their difference. The inset shows an enlarged profile around the (400) and (004) peaks.

Table 1. Refined crystal parameters and reliability factors of $BaTiO_3$ nanoparticles.

					Atomic coordinate	
Particle size	R_{wp} (%)	a (Å)	c (Å)	c/a	Ti	O(I)
$\sim\mu$m		3.9940	4.0330	1.0098		
140 nm	11.20	4.0200	4.0304	1.0026	(0.5, 0.5, 0.5340)	(0.5, 0.5, 0.0299)
(±7 nm)		(±0.0001)	(±0.0002)	(±0.000 07)		
60 nm	7.46	4.0285	4.0357	1.0018	(0.5, 0.5, 0.5201)	(0.5, 0.5, 0.0160)
(±6 nm)		(±0.0004)	(±0.0008)	(±0.0002)		
30 nm	2.78	4.0329	4.0362	1.0008	(0.5, 0.5, 0.5184)	(0.5, 0.5, 0.0061)
(±5 nm)		(±0.0006)	(±0.0012)	(±0.0003)		

for decreasing crystal size. Nevertheless, our results of XRD refinement reveal that the critical size of $BaTiO_3$ nanoparticles, which is the size of the phase transition from tetragonal to cubic at RT, may be smaller than 30 nm, that differs from the argument reported by Hoshina *et al* [11], in which the size-induced phase transition occurs between 40 and 30 nm. According to table 1, the refined atom positions in a unit cell of the tetragonal $BaTiO_3$ nanoparticles reveal less displacement of titanium and oxygen (O(I)) atoms along the c axis with decreasing particle size. It also indicates, similar to the results due to the temperature effect [22], that the Ti–O_6 octahedron shows less distortion due to less off-center displacement (Ti) resulting from the size effect.

3.2. Lattice dynamics

The Raman spectra of $BaTiO_3$ nanoparticles taken at RT were plotted in figure 4 with particle sizes of 30 nm, 60 nm, 140 nm, and >1 μm, respectively. First of all, there is a spectral dip

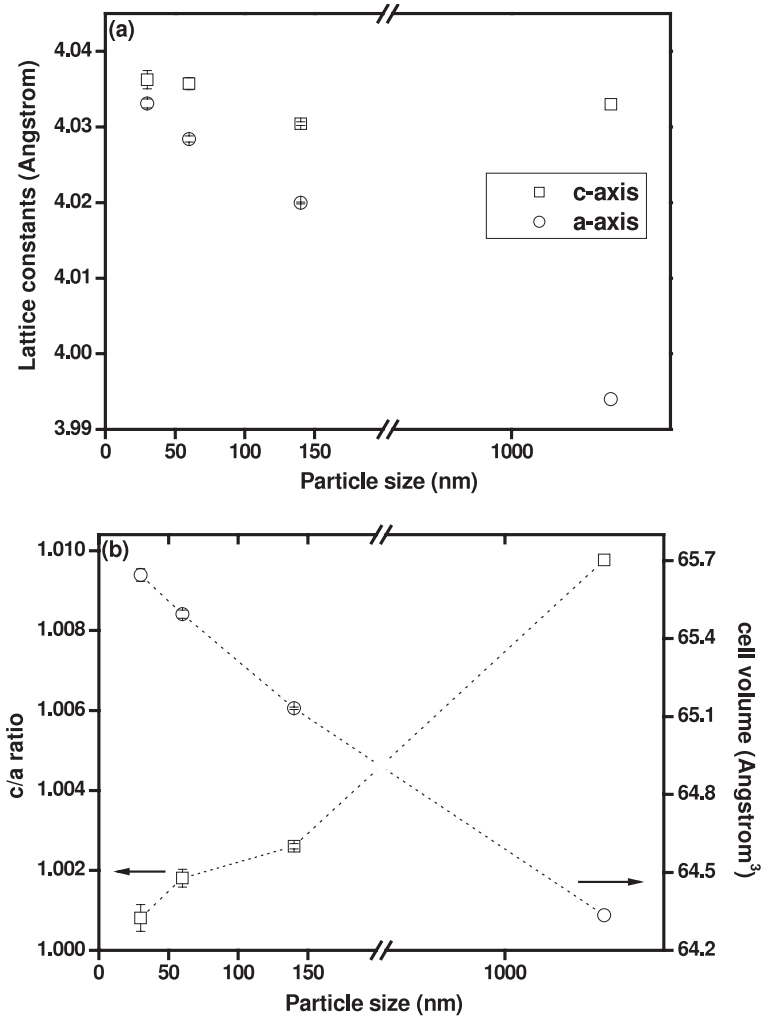

Figure 3. The lattice constants a and c of $BaTiO_3$ nanoparticles after Rietveld refinement procedure (a) and the ratio of c/a (b).

around 180 cm^{-1} for the micrometer-size sample but a spectral peak for all the nanoparticles, that is assigned to the A_1 (TO_1) phonon mode. They are basically located at the same frequency as the destructive interference dip for the bulk $BaTiO_3$. A broad band around 260 cm^{-1} attributed to the A_1 (TO_2) mode, a band at 305 cm^{-1} to $B_1 + E(TO + LO)$ modes, the asymmetric band around 520 cm^{-1} to E(TO) and A_1 (TO_3) modes, and the highest-frequency band around 720 cm^{-1} to A_1 (LO) + E(LO) phonon modes. The phonon modes at 305 and 720 cm^{-1} specific to the tetragonal phase of $BaTiO_3$ as described in [23] become weak and broad with decreasing particle size. The observed broadening and weakening of tetragonal Raman bands indicate that the crystal structure becomes progressively less tetragonal due to less displacement of Ti and O(I) atoms for the smaller particle size, which is consistent with the results of XRD. A structural model of nonpolar (cubic) and polar (tetragonal) ABO_3 crystal is shown in figure 5. Ti atoms locate at the center of the Ti–O_6 octahedron when the octahedral units are perfect in the cubic-type structure. Due to balance of the charges, the crystal is

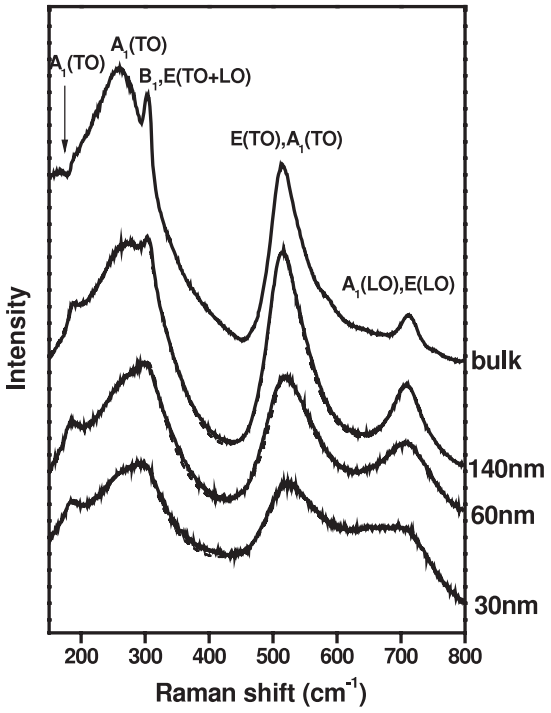

Figure 4. Size dependence of Raman spectra for $BaTiO_3$ bulk (>1 μm) and nanoparticles of diameter 140, 60, and 30 nm, respectively.

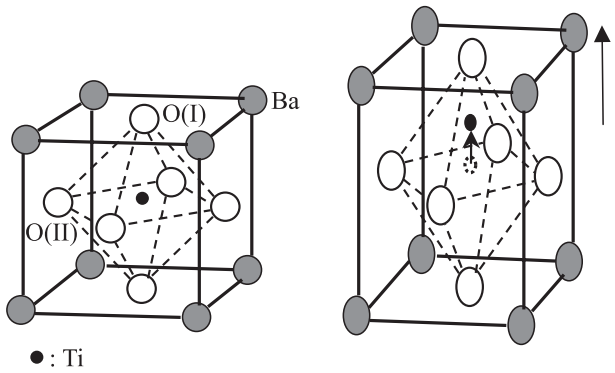

Figure 5. Structural model of the cubic (left) and tetragonal (right) phase occurring with bulk $BaTiO_3$ crystals.

nonpolar and the Raman mode is inactive. On reducing temperature, the Ti–O_6 octahedron will be somewhat distorted with off-center displacement of Ti atoms toward one of the O(I) atoms while elongating the *c*-axis to the tetragonal structure and present spontaneous dipole. The refined atom positions in a unit cell of the tetragonal $BaTiO_3$ nanoparticles reveal less displacement of titanium and oxygen (O(I)) atoms along the *c* axis with decreasing particle size so that the Ti–O_6 octahedron is less distorted or less polar due to less Ti off-center displacement resulting from the size effect.

Although we had also observed a weak peak around 810 cm^{-1} attributed to the lattice OH group [24] and a very weak band around 930 cm^{-1} (not shown here) to the oxygen vacancy [25], there are no reports on the OH groups and no direct evidence of oxygen vacancy that would influence the frequencies of the observed Raman modes. The frequency shift observed in [30] should mainly result from the interface strain introduced between $BaTiO_3$ film and substrate rather than the influence of the oxygen vacancy, because spectra (b) and (c) in figure 4 therein showed that the A_1 (LO) + E(LO) modes shifted to 715 cm^{-1} before appearance of a very weak 930 cm^{-1} band due to the oxygen vacancy. Finally, we did not observe the 1060 cm^{-1} peak attributed to $BaCO_3$ brought out by Pithan *et al* [20], so we had prevented the $BaCO_3$ related peaks located in the spectral range below 200 cm^{-1} by acetic acid washing.

Because the three A_1 (TO) modes are strongly coupled and two of them are heavily damped in the tetragonal phase of ABO_3, Sood [16] and Chaves *et al* [17] have considered three coupled A_1 (TO) modes to describe the complicated coupling phenomenon. The Raman intensity of the three coupled modes can be expressed by

$$I(\omega) = A[n(\omega) + 1]\,\mathrm{Im}[\mathbf{T}^*\mathbf{G}\mathbf{T}], \tag{1}$$

where A is a constant, $[n(\omega) + 1]$ is the Bose–Einstein factor, $\mathbf{T}$ is a vector involving Raman scattering amplitudes, and the inverse matrix response is

$$\mathbf{G}^{-1}(\omega) = \mathbf{\Omega}^2 - \omega^2\mathbf{I} - \mathrm{i}\omega\mathbf{\Gamma}. \tag{2}$$

In equation (2), $\mathbf{I}$ is the unit matrix, $\mathbf{\Omega}^2$ is the force constant matrix, and $\mathbf{\Gamma}$ is the damping matrix:

$$\mathbf{\Omega}^2 = \begin{pmatrix} \omega_1^2 & \omega_{12}^2 & 0 \\ \omega_{12}^2 & \omega_2^2 & \omega_{23}^2 \\ 0 & \omega_{23}^2 & \omega_3^2 \end{pmatrix}, \qquad \mathbf{\Gamma} = \begin{pmatrix} \Gamma_1^2 & 0 & 0 \\ 0 & \Gamma_2^2 & 0 \\ 0 & 0 & \Gamma_3^2 \end{pmatrix}. \tag{3}$$

Here ω_i and ω_{ij} $(i, j = 1, 2, 3)$ are the uncoupled mode frequencies and the coupling strengths between modes i and j. The coupling between the lowest (ω_1) and the highest (ω_3) modes was set to zero $(\omega_{13} = 0)$, to allow fewer fitting parameters; this is a reasonable approximation because they are too far from each other, having no spectral superimposition.

The asymmetric broad band around 500–600 cm^{-1} is attributed to superposition of E(TO) and A_1 (TO_3) modes, so that one has to separate them before making coupled-mode analysis. These two modes are distinguishable by polarized Raman scattering in single crystals. From the results of polarized Raman study on the epitaxial $BaTiO_3$ film by Marssi *et al* [26], the E(TO) mode is situated at the low-frequency shoulder with about one-quarter of the intensity of the A_1 (TO_3) mode. According to the process to refine the XRD data by using the GSAS, we can attain a better fitting result in XRD analysis without considering any preferred orientation. Therefore, in our powder samples the particles should possess random orientation. We have to consider the angle-dependent frequencies of these modes. It is well known that the frequency of the E(TO) mode is independent of the observing angle θ with respect to the crystallographic axes, whereas that of the A_1 (TO) mode depends upon the observing angle according to [27]

$$[\omega_{A_1}(\theta)]^2 = (\omega_{A_1})^2 \sin^2\theta + (\omega_E)^2 \cos^2\theta. \tag{4}$$

Assuming the particles are completely randomly oriented, the scattering wavevector should also randomly orient with respect to the crystallographic axis. Therefore, the observed A_1 (TO_3) frequency, after averaging over θ for equation (4), is well defined between ω_{A_1} and ω_E or $\langle\omega_{A_1}(\theta)\rangle = \sqrt{\frac{\omega_{A_1}^2 + \omega_E^2}{2}}$ and E(TO) and A_1 (TO_3) modes are separable. It is reasonable to extract the contribution of the E(TO) mode and the coupled A_1 (TO_3) mode for these randomly oriented nanoparticles. On the other hand, the A_1 (LO) mode is inseparable from the E(LO)

mode for tetragonal structure around 720 cm^{-1} when the scattering wavevector makes an angle with respect to crystallographic axes. It gives rise to mode mixing due to directional dispersion, called the 'oblique phonon'. The observed frequency shift of the angle-averaged oblique phonon in figure 4 should not depend on the observing angle θ but other effects, e.g. particle size. Therefore, other than equation (1) we added four Lorentzian functions representing background signal (Rayleigh scattering) which depends on the particle size, $B_1 + E(TO + LO)$, E(TO), and $A_1(LO_3) + E(LO)$ to fit the measured Raman spectra.

In order to attain the best fitting to our measured data, an extra band around 640 cm^{-1} has to be considered especially for 60 and 30 nm samples. This 640 cm^{-1} band was assigned to the grain-boundary regions [6] or was due to the hexagonal phase [12]. However, as aforementioned there is even better fitting with smaller R_{wp} for the size of 30 nm in XRD analysis using a single tetragonal phase; we therefore assigned the weak mode around 640 cm^{-1} to the grain-boundary regions for 60 and 30 nm samples rather than due to the hexagonal phase.

The fitting parameters of three coupled TO modes were plotted in figure 6(a), that allows us to clarify the coupling behavior of phonons with decreasing particle size. We found that the coupling strength, ω_{12}, between ω_1 and ω_2 dramatically changes from 85 cm^{-1} to nearly zero as the particle size decreases from a few micrometers to nanometers. The weaker (or zero) coupling between ω_1 and ω_2 in $BaTiO_3$ nanoparticles leads to observing a spectral peak around 180 cm^{-1} for the A_1 (TO_1) phonon mode rather than a dip at the same position. Figure 6(b) shows the plot of the as-read peak positions (hollow symbols, labeled as A_1 (TO_i), $i = 1, 2, 3$) of three A_1-symmetric TO modes from our Raman data, and those obtained from the coupled-phonon model as solid symbols. It can be seen that the size-dependent decoupled (calculated) phonon frequency ω_1 overlaps with the as-read one, again indicating weak coupling strength ($\omega_{12} \sim 0$). With less tetragonality or small c/a due to decreasing the particle size, we found that the approach of uncoupled ω_2 and ω_3 results in slightly increasing ω_{23}. The larger coupling strength ($\omega_{23} \sim 300$ cm^{-1}) repels these two modes farther such that the measured A_1 (TO_2) ($A_1(TO_3)$) peak only slightly shifts toward higher (lower) frequency upon decreasing the particle size.

Furthermore, the dynamical matrices for the LO and TO modes, which have the same form of atomic displacements in a unit cell, are related by

$$D_{mn}^{LO} = D_{mn}^{TO} + \frac{4\pi e^2}{V}\frac{Z_m^* Z_n^*}{\varepsilon_\infty(q)}, \tag{5}$$

where D represents the dynamical matrix that is proportional to the square of the vibration frequency, V is the volume of the unit cell, $\varepsilon_\infty(q)$ is the optical dielectric constant, and Z^* is the Born effective charge of the corresponding vibration. The Coulomb interaction would play an important role in the behavior of LO–TO splitting.

Figure 7 shows the peak positions of A_1 (LO) and A_1 (TO_1) modes versus $BaTiO_3$ particle size. We observed that besides the expected softening of both A_1 (LO) and A_1 (TO_1) modes there is a decreasing trend of LO–TO splitting as the particle size decreases from >1 μm to 30 nm. Since Ba-based ABO_3 perovskites basically possess ionic bonding [14, 28–30], the Born effective charge would not be influenced by change of structure [15, 29]. From the results of figure 3(b), that the unit-cell dimension of $BaTiO_3$ particles increases with the particle decreasing from micrometer size to 30 nm, we would expect reducing LO–TO splitting. Relatively, we previously reported that the tetragonality declines with unit-cell volume diminishing as x changes from 1 to 0.7 in polycrystalline $Ba_xSr_{1-x}TiO_3$ [7]. Change of unit-cell volume was considered the dominant mechanism of increasing the LO–TO splitting in this system with negligible change of effective charge due to the substitution. In this study we directly observed the decreasing LO–TO splitting with the decline of tetragonality by decreasing the size of $BaTiO_3$ nanoparticles, which causes expansion of the unit-cell volume.

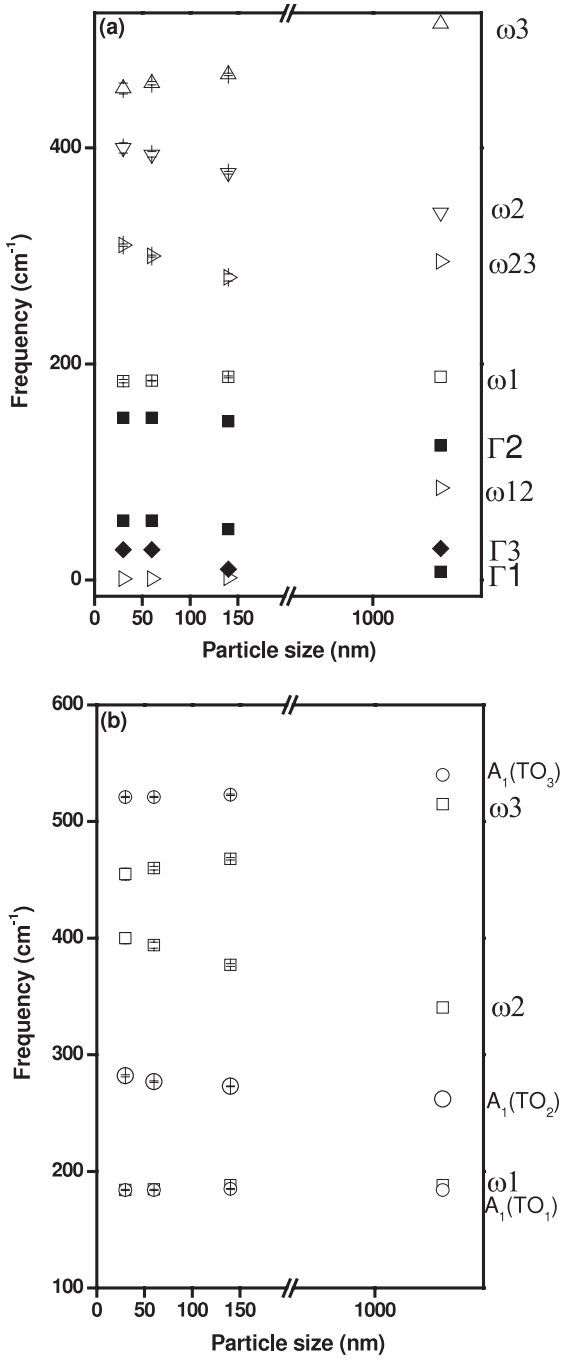

Figure 6. The fitted parameters using the coupled-phonon model as a function of particle size. (a) The as-read peak positions from the data and (b) the decoupled frequencies.

Based on equation (5), we normalized the square difference of phonon frequencies of $A_1(LO_3)$ and A_1 (TO_1) for nanometer size samples to that of micrometer size and plotted them

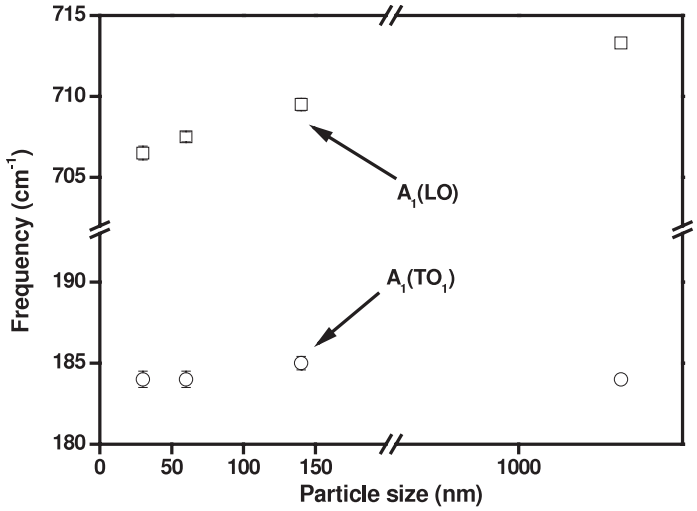

Figure 7. The LO–TO splitting of the A_1 (LO_3) and A_1 (TO_1) modes as a function of particle size.

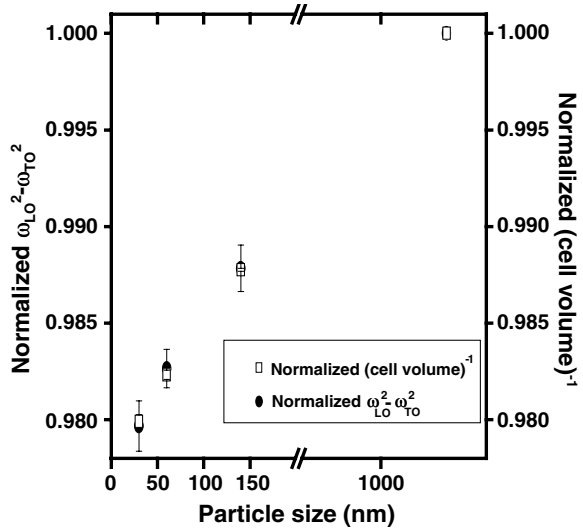

Figure 8. Normalized square difference of phonon frequencies of $A_1(LO_3)$ and A_1 (TO_1) (solid circles) and normalized reciprocal of unit-cell volume (open squares) for nanometer size samples to micrometer size.

in figure 8 to compare with the normalized reciprocal of unit-cell volume also to that of the micrometer size. This shows that the normalized square difference of phonon frequencies of $A_1(LO_3)$ and A_1 (TO_1) almost coincides with the normalized reciprocal unit-cell volume with less than 2% deviation. This result indicates that the value of $\frac{4\pi e^2 Z_m^* Z_n^*}{\varepsilon_\infty(q)}$ is a constant, namely, the Born effective charges should not be influenced by change of structure or size, and the change of unit-cell volume is the dominant mechanism for the tendency of LO–TO splitting in the $BaTiO_3$ system without the complication of ion replacement.

4. Conclusion

The size effect on structure for $BaTiO_3$ nanoparticles synthesized by the glycothermal method has been investigated using FESEM, high-resolution synchrotron XRD, and Raman spectroscopy. We further applied a single-tetragonal-phase model to refine the crystal structure and the coupled-phonon model to analyze the coupled A_1 (TO) modes upon particle size decreasing from 140 to 30 nm. We explained that the weak strength of coupling between A_1 (TO_1) and A_1 (TO_2) leads to a change from a spectral dip at 180 cm^{-1} for the A_1 (TO_1) phonon to a peak at the same position and found that the approach of uncoupled ω_2 and ω_3 with less tetragonality due to decreasing particle size results in slightly increasing ω_{23}. The larger coupling strength repels these two modes farther so that there is less reduction in spectral separation. According to the results of decomposition, we also observed the decreasing LO–TO splitting with the decline of tetragonality and expansion of the unit-cell volume. Moreover, the change of unit-cell volume is the dominant mechanism for the tendency of the LO–TO splitting in the $BaTiO_3$ system without the complication of ion replacement.

Acknowledgment

The work was supported by grant no. NSC 96-2628-M-009-001 from the National Science Council, Taiwan.

References

[1] Cross L E 1984 *Am. Ceram. Soc. Bull* **63** 586–90
[2] Yoon D H and Lee B I 2004 *J. Eur. Ceram. Soc.* **24** 753
[3] Pirc R and Blinc R 2004 *Phys. Rev.* B **70** 134107
[4] Íñiguez J and Vanderbilit D 2002 *Phys. Rev. Lett.* **89** 115503
[5] Damjanovic D, Brem F and Setter N 2002 *Appl. Phys. Lett.* **80** 652
[6] Venkateswaran U D, Naik V M and Naik R 1998 *Phys. Rev.* B **58** 14256
[7] Kuo S Y, Liao W Y and Hsieh W F 2001 *Phys. Rev.* B **64** 224103
[8] Frey M H and Payne D A 1996 *Phys. Rev.* B **54** 3158
[9] Tsunekawa S, Ito S, Mori T, Ishikawa K, Li Z Q and Kawazoe1 Y 2000 *Phys. Rev* B **62** 3065
[10] Zhao Z, Buscaglia V, Viviani M, Buscaglia M T, Mitoseriu L, Testino A, Nygren M, Johnsson M and Nanni P 2004 *Phys. Rev.* B **70** 024107
[11] Hoshina T, Kakemoto H, Tsurumi T, Wada S and Yashima M 2006 *J. Appl. Phys.* **99** 054311
[12] Yashima M, Hoshina T, Ishimura D, Kobayashi S, Nakamura W, Tsurumi T and Wada S 2005 *J. Appl. Phys.* **98** 014313
[13] Ishikawa K and Uemori T 1999 *Phys. Rev.* B **60** 11841
[14] Cohen R E 1992 *Nature* **358** 136
[15] Zhong W, King-Smith R D and Vanderbilt D 1994 *Phys Rev. Lett.* **72** 3618
[16] Sood A K, Chandrabhas N, Muthu D V S and Jayaraman A 1995 *Phys. Rev.* B **51** 8892
[17] Chaves A, Katiyar R S and Porto S P S 1974 *Phys. Rev.* B **10** 3522
[18] Buscaglia V, Buscaglia M T, Viviani M, Ostapchuk T, Gregora I, Petzelt J, Mitoseriu L, Nanni P, Testino A, Calderone R, Harnagea C, Zhaof Z and Nygren M 2005 *J. Eur. Ceram. Soc.* **25** 3059
[19] Junga Y J, Lima D Y, Nhob J S, Chob S B, Rimanc R E and Leed B W 2005 *J. Cryst. Growth* **274** 638
[20] Pithan C, Shiratori Y and Waser R 2006 *J. Am. Ceram. Soc.* **89** 2908
[21] Yoon S, Baik S, Kim M G and Shin N 2006 *J. Am. Ceram. Soc.* **89** 1816
[22] Kwei G, Billinge S J L, Cheong S W and Saxton J G 1995 *Ferroelectrics* **164** 57
[23] Naik R, Nazarko J J, Flattery C S, Venkateswaran U D, Naik V M, Mohammed M S, Auner G W, Mantese J V, Schubring N W, Micheli A L and Catalan A B 2000 *Phys. Rev.* B **61** 11367
[24] Busca G, Buscaglia V, Leoni M and Nanni P 1994 *Chem. Mater.* **6** 955
[25] Guo H Z, Chen Z H, Chenf B L, Lu H B, Liu L F and Zhou Y L 2005 *J. Eur. Ceram. Soc.* **25** 2347
[26] Marssi M E, Marrec F L, Lukyanchuk I A and Karkut M G 2003 *J. Appl. Phys.* **94** 3307
[27] Burns G and Scott B A 1973 *Phys. Rev.* B **7** 3088
[28] Kuroiwa Y, Aoyagi S and Sawada A 2001 *Phys. Rev. Lett.* **87** 217601
[29] Kuo S Y, Li C T and Hsieh W F 2002 *Appl. Phys. Lett.* **81** 3019
[30] Jan J C, Tsai H M, Pao C W, Chiou J W, Asokan K, Krishna Kumar K P, Pong W F, Tang Y H, Tsai M H, Kuo S Y and Hsieh W F 2005 *Appl. Phys. Lett.* **87** 012103